BIOLOGICAL TRANSLATION: BIOLOGICAL MATERIALS SCIENCE AND BIOINSPIRED DESIGN

Fabrication and Testing of Bioinspired Composites with Curved Multilayer Microstructures

XIN YING CHAN,[1] ZHENG HAO NG,[1] LIZHI GUAN,[1] HONGYING HE,[1] SLOCHA SAPASAKULVANIT,[1] PEIFANG DEE,[1] and HORTENSE LE FERRAND [1,2,3]

1.—School of Mechanical and Aerospace Engineering, Nanyang Technological University, 50 Nanyang Avenue, Singapore 639798, Singapore. 2.—School of Materials Science and Engineering, Nanyang Technological University, 50 Nanyang Avenue, Singapore 639798, Singapore. 3.—e-mail: hortense@ntu.edu.sg

Natural strong and stiff composites exhibit complex microstructures that are responsible for their outstanding strength, stiffness, and toughness. Although horizontal nacre-like microstructures have demonstrated great potential in synthetic composites, they only demonstrate high performance along a specific loading direction. Here, we study how complex curved multilayered microstructures made of aluminum oxide microplatelets in a soft polymeric matrix can possess a combination of both stiffness and toughness. To do so, magnetically-assisted slip casting was used to direct the microplatelets into periodic orientations, as reported in previous studies, while the porous substrate used for the slip casting was designed with a raised step of different heights to control the shape of the oriented layers. The samples' microstructures achieved in-plane modulation of the microplatelet orientation, and the mechanical properties under compression were enhanced compared to samples with layers parallel to the horizontal plane. The microstructured design proposed here could be used to make more resilient bioinspired composites.

INTRODUCTION

Natural materials exhibit complex and intricate microstructures that confer them outstanding properties.[1,2] In particular, natural mineralized materials with more than 80 vol.% of solids, also referred to as natural ceramics, exhibit exceptional combinations of strength and toughness. Several bioinspired ceramics have been developed to leverage the strengthening and toughening mechanisms found in these natural materials to transfer them to synthetic materials.[3,4] The gold standard of bioinspired materials is nacre-like composites which contain a brick-and-mortar arrangement of plate-like grains, similar to that of natural nacre (Fig. 1A).[5,6] However, although nacre-like materials exhibit exceptional performance, this is only true under a specific loading direction, namely perpendicularly to the brick-and-mortar structure. When subjected to various loading directions in realistic conditions, monolithic horizontal alignments in nacre-like microstructures may therefore not be the most performant. Therefore, it is necessary to develop microstructured materials that display enhanced performance in multiple directions.

Since natural materials also come in 3D shapes and are subjected to diverse loading scenarios, they also present microstructural designs that can serve as inspiration for high-performance technical materials. For example, the shells of land snails and seashells, and the dactyl club of stomatopods, are composite materials with more than 80 vol.% inorganic building blocks, microplatelets, or microfibers, which exhibit high strength and toughness. In these materials, the building blocks are arranged into multi-layered, hierarchical structures and in curved macroscopic shapes (Fig. 1B–D). The high concentration of minerals confers high strength and stiffness to the materials, whereas the hierarchical microstructure generates extrinsic toughening
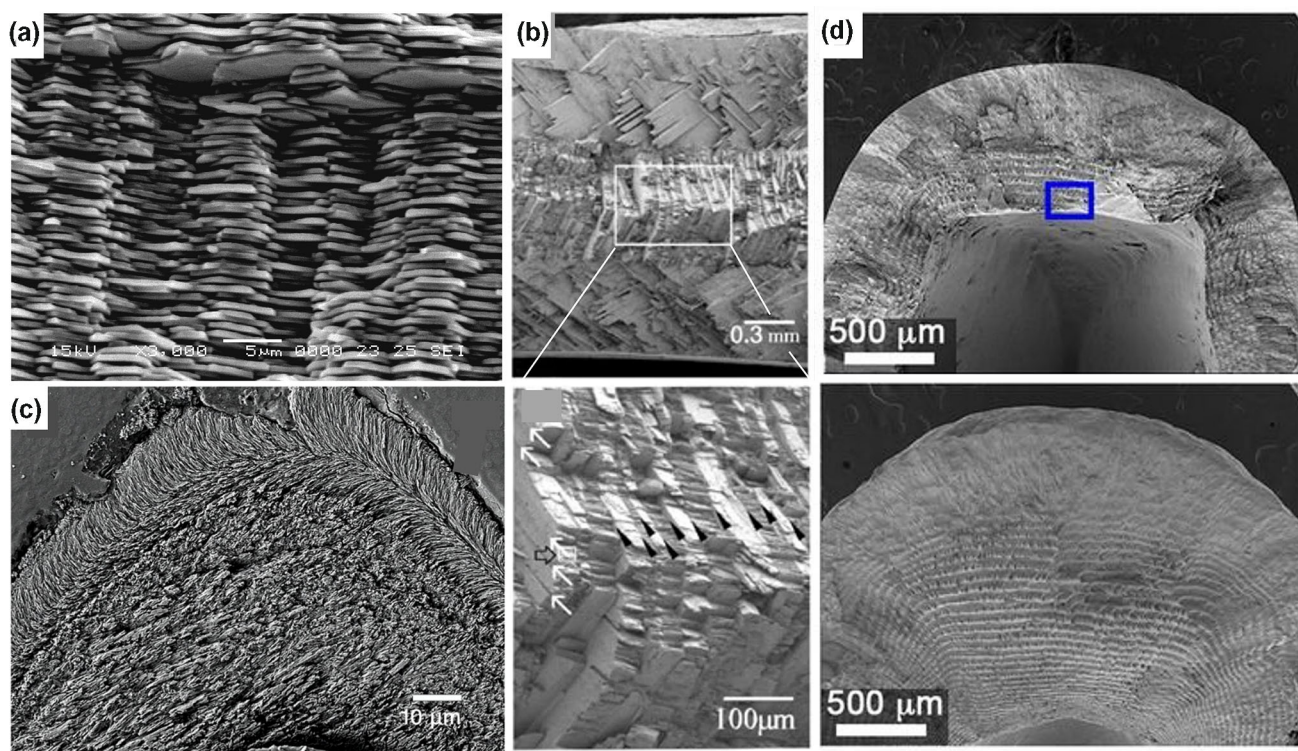
Fig. 1. Complex hierarchical microstructures of natural materials. Electron micrographs of: (A) brick-and-mortar assembly of $CaCO_3$ microplatelets in the nacreous layer of *Haliotis discus hannai*; (B) curved multilayer structures in the shell of the snail *Camptoceratops priscus*; reprinted from Ref. 7 under the terms of the Creative Commons CC BY license; (C) cross-lamellar structure in the shell of *Strombus gigas*; reprinted with permission from Ref. 8. (D) curved and multilayer Bouligand structures in the dactyl club of the mantis shrimp; reprinted with permission from Ref. 9.

mechanisms such as crack bridging, microcracking, etc. Furthermore, the building block orientations vary between the layers to redistribute the stresses as well as to deviate cracks.[10] In addition, it is observable that the building blocks' orientation varies in plane such that the layers curve along with the outer shape of the structure, providing the required reinforcement in 3D shapes. This is unlike the gold-standard nacre-like microstructure in synthetic composites where the building blocks are all horizontally aligned throughout the entire piece. Although the formation of complex material microstructures in nature likely stems from the natural growth of the organism and their primary goal is to protect internal tissues, such microstructures may also play a part in improving the mechanical properties of the material. Furthermore, apart from specialised parts such as the dactyl club, the loading states in most other natural shells are unlikely to be uniaxial due to natural phenomena, such as tides, wind, predators' attacks, and movements of the organism itself. Loads with varied magnitude and directions are likely to be imposed on the structure throughout its lifetime. Therefore, natural materials are more likely to possess mechanical resistance in multiple axes. Taking inspiration from complex multilayer microstructures could therefore help us to design custom-shaped parts with enhanced performance under multiple loading conditions.

Multilayer bioinspired composites with complex hierarchical microstructures have been developed in the past, showing how the microstructural arrangement unlocks toughening mechanisms despite the high stiffness of the parts. For example, a variety of Bouligand structures, where aligned fibers are skewed at an angle between each layer were made, showing increased impact resistance when the angle is about 10–20°.[11,12] Hexagonal and stochastic structures within layers of ceramics have been shown to improve the toughness and stiffness of ceramic systems by up to 330% under repeated impact.[13] Complex cross-lamellar structures mimicking that of conch shells have been made, and were found to significantly improve the damage tolerance of Si_3N_4-BN composites by about 7 times.[14]

Previous work explored the microstructure–properties relationships in multilayer microstructured assemblies, where Al_2O_3-polydimethyl siloxane (PDMS) composites have been fabricated using magnetically-assisted slip casting (MASC).[15] MASC is a method where magnetically functionalized microplatelets are distributed into a low-viscosity liquid, typically water with a low concentration of

polymer binder, and slip-cast onto a porous substrate. During the slip casting, a low rotating magnetic field is applied to orient the magnetically functionalized microplatelets, while the removal of the water through the porous substrate consolidates the structure. As the water is gradually removed during slip casting, the magnetic field can be set at various angles to obtain multilayered structures with microplatelets consolidated in the specified orientation in each layer.[16,17] After further drying in the oven, the porous microstructured samples were infiltrated with PDMS and tested under compression. It was found that multilayered structures with alternating horizontal and vertical microplatelet alignment possessed a superior combination of stiffness, strength, and toughness compared to monolithic horizontal or vertical ones. This is because horizontal microplatelet alignments resulted in the lowest stiffness while vertical microplatelet alignments were stiff but had poor toughness. Structures with alternating layers of vertical and horizontal alignment displayed a good balance between stiffness and toughness and were therefore preferred over monolithic structures. Since the layers built in MASC follow the contour of the porous substrate, MASC can be used to build curved multilayered structures by using a curved gypsum substrate. An example of multilayer microstructured ceramics with layers following a wavy gypsum surface has been produced previously.[18]

In this work, we used MASC to fabricate Al_2O_3-PDMS composites with curved multilayer microstructures with an angle of 90° between alumina microplatelet orientation in each layer, and tested the samples under compression. To realize the curved layers, the gypsum substrate was designed with a step of controlled height. The fabrication process is described in detail, and the effects of the step height on the layer height, in-plane modulation, and microstructure were studied. Compression tests were carried out and the strength, stiffness, toughness and cracking patterns are compared. The results and challenges are then discussed. This study shows microstructures with unprecedented complexity in alumina-PDMS composites and investigates how such complexity contributes to changes in the mechanical properties of the material. Compared to previous work, here we leverage the capabilities of an established processing method to push it further and design microstructured samples with augmented properties. The microstructures with the highest curvatures had vertical and horizontal layers next to each other. In comparison with similar composites from the previous study where there were only horizontal layers, the composites with curved layers exhibited an increase in the stiffness while the strength and toughness remained similar. This result could be transposed into alumina ceramics or alumina composites with a stronger polymeric phase, such as epoxy, to enhance their properties.

MATERIALS AND METHODS

Preparation of the Slurry for Magnetically Assisted Slip Casting

Following the method used in the previous study,[15] the slurry used to make the composites using MASC was prepared. First, Al_2O_3 platelets (RonaFlair White Sapphire; Merck, Germany) of 10 μm diameter were stirred with 0.01 vol.% Fe_3O_4 nanoparticles (EMG-705; 10 nm diameter; Ferrotec) in neutral pH water for about 2 days. Magnetized Al_2O_3 (m-Al_2O_3) platelets were produced from this process due to the complete electrostatic adsorption of the Fe_3O_4 nanoparticles on the surface of the Al_2O_3 platelets. The m-Al_2O_3 platelets were subsequently filtered out, rinsed with water and ethanol, and dried in an oven (IKA 125; Malaysia) at 48 °C. Next, 20 vol.% of the dried m-Al_2O_3 was dispersed in water with a drop of surfactant (Dolapix CE64; Zschimeer & Schwarz, Germany) to form the slurry. For thorough dispersion, the slurry was mixed with a vortex and a probe ultrasonicator (Sonopuls HD 4100; Bandelin, Germany) 5 times at 20% amplitude, for 2 min each time. Thereafter, 5 wt.% of polyvinyl pyrrolidone (MW = 360,000; Sigma-Aldrich, China) was added and left to stir until dissolved.

Fabrication of the Porous Substrate with a Step

Gypsum (Ceramix standard; Germany) prepared following the instructions from the manufacturer was used to fabricate a base piece with a step of controllable height, h_{step}. First, a negative mold of the step feature made of PDMS was prepared (Fig. 2A). To do so, a computer-aided design (CAD) model was created, with the inverted gypsum model at its center. The CAD model was made with two separate parts for easy demolding later. Using CAD, the height of the step in the gypsum could be easily controlled. The model was then 3D-printed in polylactic acid (filament 1.75 mm red; 3D Aura, Singapore) using the printer Prusa I3 (MK3S MMU2S; Czech Republic). The printed parts were secured together, and the cavity was filled with PDMS (SYLGARD™ 184 Silicone Elastomer; Dow Corning, USA), prepared according to the manufacturer's instructions. The PDMS was degassed in a vacuum oven for 5 min and finally cured for 48 h in an oven at 48 °C to produce a flexible negative mold. Gypsum was filled into the PDMS molds and left to dry until hard and brittle. The hard and brittle gypsum substrates with step heights of h_{step} from 0 to 8 mm (Fig. 2B, C) were demolded easily from the flexible PDMS, then dried fully in the oven at 48 °C. Finally, the side walls of the slip-casting mold were formed by attaching a hollow plastic cylinder to the gypsum base using Parafilm.

Furthermore, the thicknesses h_{base} of the gypsum base under the step of the gypsum could also be
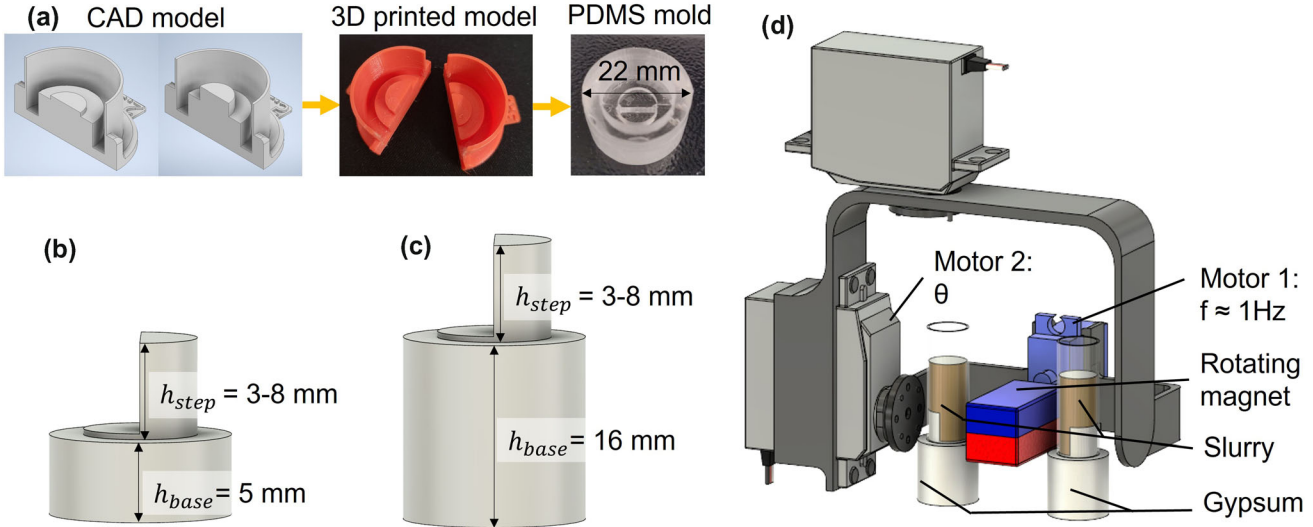
Fig. 2. (A) Fabrication mold for porous gypsum base by CAD design, 3D printing, and then molding. (B) Schematic of thin gypsum mold with 5 mm h_{base} and 3–8 mm h_{step}. (C) Schematic of thick gypsum mold design with 16-mm h_{base} and 3- to 8-mm h_{step}. (D) Schematic depicting the magnetic assembly setup and the placement of two samples being made at the same time using the MASC process. Motor 1 controls the rotation frequency (f) of the magnet while Motor 2 controls the alignment of the platelets.

controlled. We produced gypsum with h_{base} of 5 and 16 mm to compare the effect of the porous base on the layer thicknesses in the samples.

Magnetically Assisted Slip Casting

A programmable magnetic alignment setup devised in a previous study (see Supplementary Fig. 2),[15] that comprised two motors assembled with a 3D-printed frame (Fig. 2D) was used to carry out MASC. The setup was programmed to align the platelets vertically and horizontally in alternating layers, with a 1-min interval for each layer. This time interval was chosen such that adjacent layers were thick enough to be distinguished optically, for the ease of taking measurements on the pitch and layer thickness. In practice, two identical samples were produced at the same time using the setup (Fig. 2D). The magnetic field at the position of the sample was measured to be 10–50 mT (GM07 with transverse probe; Hirst Magnetic Instruments) and was applied during the entire slip casting time, of about 1 h. All the samples were cast using freshly made gypsum to ensure uniformity in the rate of water removal in the samples. After the gypsum removed the water from the slurry, the samples were further dried in an oven at 48 °C for 48 h before carefully unmolding, then dried in the oven for another 48 h.

PDMS Infiltration

After drying, the samples made by MASC are porous. A composite was made by infiltration of PDMS diluted with 50 wt.% silicone oil (10 cSt Silicone oil; Sigma-Aldrich, Singapore) as the

polymer matrix. The samples were submerged in PDMS and placed in a vacuum oven for about 2 h, until no more air bubbles developed. The vacuum improved the infiltration efficiency by creating a pressure difference that quickly draws out the air pockets from the porous samples, allowing the PDMS to fill up the pores. The dilution in silicone oil ensured low viscosity for efficient infiltration. The samples were then cured at 48 °C for 72 h in the oven. The top and bottom surfaces of the infiltrated samples were polished flat using sandpaper (Struers, USA), to ensure minimal stress concentration during the subsequent compression tests.

Characterization and Testing

Optical Microscopy

A portable digital microscope (Dino-lite AM7915MZTL; × 10–140 magnification) was used to image the macroscopic features of the samples. The layer height h_{layer} and pitch p in the cast samples were measured from the contrast in colors between adjacent layers of microplateletes with different orientations.[19] The measurements were repeated on three independent samples to ensure reproducibility.

Electron Microscopy

To observe their microstructure, dried samples were broken into two segments, A and B. Segment A was further broken in two (Fig. 3A) and the fractured cross-section was observed under a scanning electron microscope (SEM; JSM-5600LV; JEOL, Singapore) after sputter-coating with gold for 120 s.
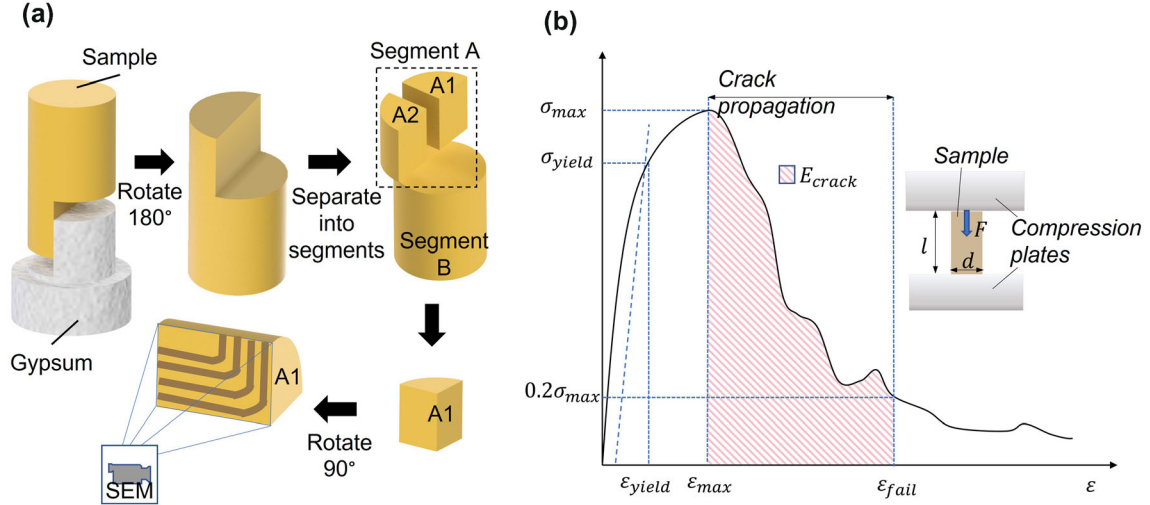
Fig. 3. (A) Schematic of sample segmented for observation of microstructure under SEM. The sample was de-molded and fractured to reveal the cross-section of segment A. (B) Schematic of mechanical properties characterization from compression testing.

Compression Test

Unconfined compression tests were conducted on both segments A and B of the samples, with a constant strain rate of 1%/min using a universal tester (Instron 3366, Singapore) with a 500-N load cell. Three samples were tested for each configuration. Figure 3B shows how the samples were characterized using the engineering stress–strain curves. The engineering stress σ and strain ε values were calculated as shown in Eqs. 1–3:

$$\sigma = \frac{4F}{\pi d^2} \text{ (for segment B)}, \tag{1}$$

$$\sigma = \frac{8F}{\pi d^2} \text{ (for segment A) and} \tag{2}$$

$$\varepsilon = \frac{\Delta l}{l}, \tag{3}$$

where l is the total height of the sample initially, F the load applied, and d the diameter of the sample. σ_{yield} was obtained graphically based on 0.2% offset yield strain $\varepsilon_{\text{yield}}$. The maximum stress, σ_{max}, was identified as the peak of the stress–strain curve, and the corresponding strain was recorded as ε_{max}. $\varepsilon_{\text{fail}}$ was defined to be strain corresponding to the point where the stress drops to 20% of σ_{max} where failure can be identified by a significant drop in stress. The initiation and propagation of cracks dissipated energies, which were represented by the area under the stress–strain curve from the start to ε_{max}, and ε_{max} to $\varepsilon_{\text{fail}}$ respectively, following:

$$E_{\text{pre-crack}} = \int_0^{\varepsilon_{\text{max}}} h \, d\varepsilon \tag{4}$$

$$E_{\text{crack}} = E_{\text{diss}} - E_{\text{pre-crack}}. \tag{5}$$

The compression test was recorded with a portable digital microscope, and images at specific timings were captured to examine the cracking behavior of the samples under loading. Student's t test was conducted with a 95% confidence interval to verify if there were significant differences between the mechanical properties of the tested samples.

RESULTS

Fabrication of Curved Microstructured Multilayers

MASC effectively creates bioinspired multilayer structures by slip-casting a concentrated slurry of magnetized ceramic microplatelets onto a porous substrate under an external magnetic field.[15,16,18,20] To obtain ceramic structures with curved multilayers, MASC was carried out on custom-designed gypsum molds with the rotating magnet alternating between 0° and 90° after every minute. The 0°/90° directions were chosen to create alternating layers of vertically and horizontally aligned Al_2O_3 microplatelets in the scaffolds. Here, we used a gypsum substrate with a thick base and a step of height h_{step} of 3–8 mm to create the curved multilayers (Fig. 4). The scaffolds were then infiltrated with PDMS as the polymer matrix to form composites.

As the water-based slurries of Al_2O_3 microplatelets were consolidated and dried by the gypsum molds, the controlled orientation of the microplatelets was achieved by rendering them magnetically responsive using an Fe_3O_4 coating and applying rotating magnetic fields.[20] In MASC, the water-based slurry containing the magnetically responsive microplatelets is poured onto the porous gypsum substrate while the rotating magnetic field aligns
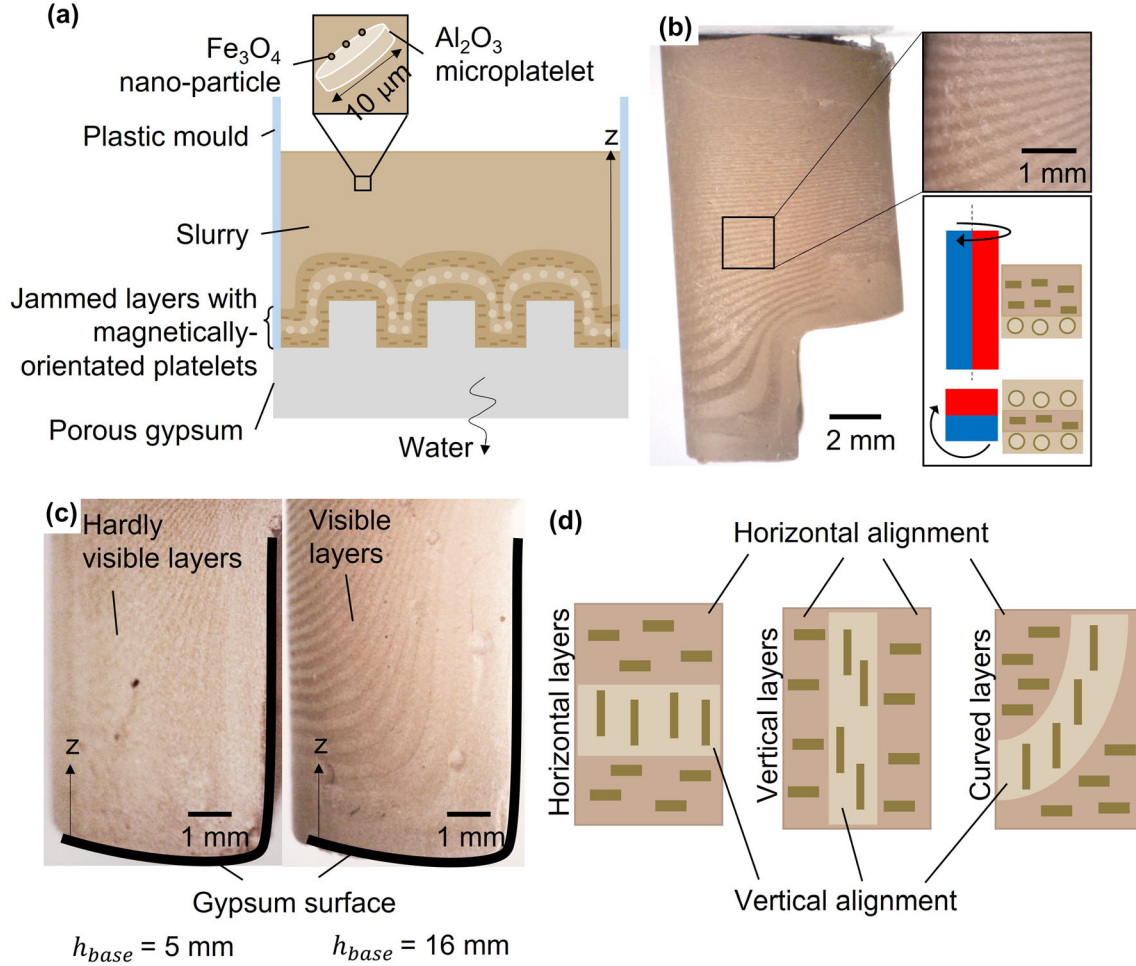
Fig. 4. (A) Schematics of the slip casting mechanism in microstructured samples with curved layers. Layers form following the contour of the base porous gypsum as the water is removed from the slurry, and platelets aligned by a magnet are set in position. (B) Optimized visibility of the layers, by setting the position of the magnet as indicated on the schematics. (C) Samples cast using the gypsum with a 5-mm h_{base} had thin fine layers that were barely visible, while samples cast using the thicker 16-mm h_{base} had thicker visible layers. (D) Schematic of the layers and platelet alignment in each layer of the curved samples (Color figure online).

the microplatelets. The continuous water removal by capillary action through the pores of the gypsum consolidates the slurry into a thick cake starting from the regions closest to the gypsum. In the cake, the microplatelets are jammed and fixed into their orientation as the slurry dries. In the dried scaffold, the Al_2O_3 microplatelets are held together by a small amount of polymer binder. The continuous water removal may be described by the casting kinetics:

$$z = a\sqrt{t}, \qquad (6)$$

with t the casting time, z the cake thickness, and a a constant that depends on the gypsum's capacity to absorb water and the tortuosity in the deposited cake. Thus, the layers conform to the gypsum substrate until a certain height above which the cake front becomes horizontal again (Fig. 4A). To create layers with 0–90° microplatelet orientations, it suffices to vary the magnetic field orientation in a timewise manner. When the direction of the

magnetic field is changed, the platelet alignment in the jammed cake remained fixed, while the platelets suspended in the liquid slurry above the cake align with the new direction of the magnetic field. As the cake increases in thickness, the microstructured layers pile up according to the contour of the gypsum.

The microstructured layers were visible to the naked eye due to the color contrast between the layers.[19] Indeed, the microplatelets reflect more light on their basal plane than on their edges. Looking from the side of the samples, the layers with 0° orientation (horizontal microplatelet alignment) appeared darker than those with 90° orientation (vertical microplatelet alignment). To optimize the visibility of the layers, the magnet was positioned so that the vertically oriented platelets were facing the edge of the step. This gives the greatest contrast between the colors of the layers (Fig. 4B). The thickness h_{layer} of the layer built at a distance z from the gypsum surface,
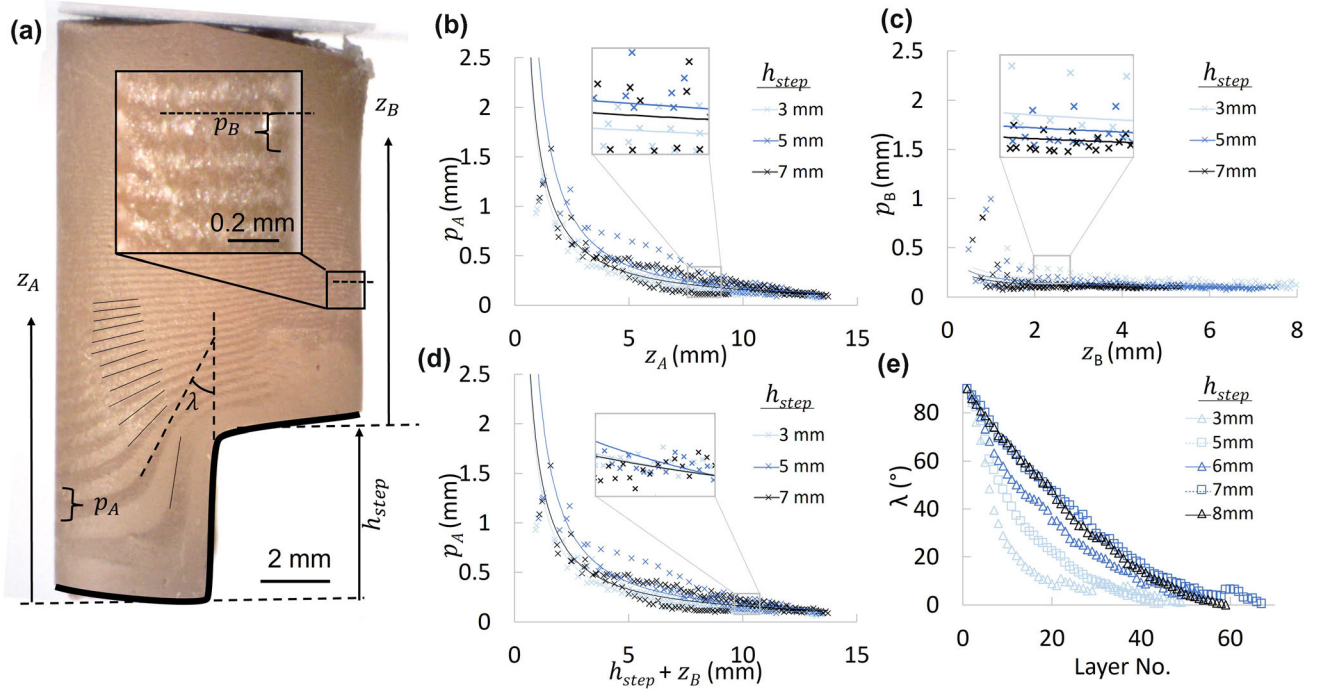
Fig. 5. (A) Schematic showing the measurement of pitches p_A and p_B and tilt angle λ. (B) Variation of the pitch p_A as a function of the layer height z_A for steps of height 3, 5, and 7 mm. (C) Variation of the pitch p_B as a function of the layer height z_B for various step heights. (D) Various of p_B as a function of $z_B + h_{step}$ for various step heights. (E) Tilt angle λ as a function of the layer number increases for h_{step} from 3 mm to 8 mm.

depends on the time t_{jam} required for the cake to reach thickness of z, following:

$$t_{jam} = \frac{z^2}{a^2}. \tag{7}$$

Therefore, the further from the gypsum, the longer the time required for jamming to occur. For a fixed time interval t_B between each rotation of the magnet from 0 to 90°, the time for jamming increases and h_{layer} decreases, leading to a structure with a pitch p following:[16]

$$p = \frac{a^2 \cdot t_B}{2 \cdot z}. \tag{8}$$

Furthermore, a is proportional to the water absorption rate by the gypsum. Therefore, a quick casting speed due to the fast absorption of the water in the gypsum leads to a small t_{jam} and a large p.

To effectively prepare curved microstructured layers, we varied the casting kinetics by tuning the thickness of the gypsum base h_{base} (Fig. 4C). It was found that gypsum that was too thin led to fast saturation of the water in the gypsum and significantly increased t_{jam}, leading to hardly visible layers (see SI Supplementary Fig. 1 for cross-sections of samples made with various gypsum thickness, and associated supplementary text). In turn, using a h_{base} of about 16 mm, the layers were thick and were easily visible. The samples obtained showed curved multilayers with decreasing thickness and following the step of the gypsum, as expected.

With this fabrication scheme, we could therefore create multilayer structures with controlled orientation of microplatelets in each layer and with curved geometries. The curved layers comprise regions of vertical and horizontal layers, and the microplatelets were aligned in alternating layers of vertical and horizontal microplatelet alignment (Fig. 4D). Schematically, the sample looks as if horizontal layers and vertical layers are side-by-side but with a continuous transition from horizontal to vertical. A thick gypsum base substrate of 16 mm and a magnet positioned on the side of the step allowed the creation of clear optically visible layers. Following this, we varied the step height in the gypsum substrate and studied its influence on the multilayers.

Optical Characterization of the Curved Multilayers for Different Step Heights

To determine how the step feature in the gypsum substrate influenced the microstructure in the cast samples and created curved microstructured layers, the step height h_{step} was varied from 3 to 8 mm. The pitch p of the microstructure and tilt angle λ in the built layers were measured (Fig. 5).

Each specimen was divided into two segments, a half-cylinder segment A and a cylindrical segment B. Segment A, next to the step, generally featured thicker layers with large curvatures. Segment B, on top of the step, had thinner layers with smaller curvature. The pitches p_A and p_B of the structure in these two segments, which are the thickness of two

consecutive layers, a light and a dark layer, were measured by image analysis (Fig. 5A). Furthermore, the samples displayed curved layers where curvature was quantified by measuring the tilt angle λ of each layer with respect to the vertical as indicated in Fig. 5A. λ was measured by fitting a straight line between the two angled sections in the layers, with $\lambda = 0°$ meaning that the layer is completely vertical and $\lambda = 90°$ that the layer is completely horizontal. This tilt measurement was chosen instead of measuring a radius of curvature as the layers did not follow the shape of a simple arc.

As expected from Eq. 7, the pitch p_A decreased with z_A (Fig. 5B). h_{step} had no influence on p_A, likely because the layer thickness depends on the timestep variation of the magnetic field orientation t_B, which was fixed at 1 min. Similarly, p_B decreased with z_B (Fig. 5C). However, p_B was generally much lower compared to p_A. Although the distance to the surface of the gypsum substrate is the same, it can be hypothesized that the water from the slurry deposited in segment A imbibed the gypsum below segment B, slowing the casting kinetics and led to a higher t_{jam}. This explains why h_{step} has an influence in this segment, with a smaller h_{step} leading to larger a pitch p_B (inset in Fig. 5C). We also plotted p_B as a function of $z = h_{step} + z_B = z_A$ (Fig. 5D). The plot obtained also differs from that of p_A plotted as a function of z_A, indicating a different absorption kinetic in the two segments.

The step height of the gypsum substrate had also a large effect on the curvature of the layers, as intended. For all h_{step}, λ decreased as more layers built up away from the gypsum. As discussed above, the initial layer thickness next to the step (segment A) was larger than above the step (segment B). Therefore, as the cake front of segment A progresses further away from the gypsum surface, the jamming time t_{jam} gradually increased until it matched with the jamming time on segment B. Furthermore, the smaller the h_{step}, the quicker λ drops towards 0. Therefore, a higher h_{step} is required to form a large number of curved layers from segment A and into segment B. However, the increase in step size was effective in increasing λ only up to $h_{step} = 7$ mm. Samples with $h_{step} = 7$ mm and $h_{step} = 8$ mm had similar λ. To further increase the step height, the thickness of the gypsum substrate h_{base} could be increased to accelerate the casting kinetics.

Nevertheless, we found the approach with the substrate with a base thickness of 16 mm and a step feature to be effective in creating curved layers. A higher step up to 7 mm in the gypsum led to a higher curvature of the layers in segment A. In the following, we look more closely at the microstructure obtained in these multilayer structures.

In-Plane Modulation of the Microplatelets' Orientation

Contrary to samples fabricated on a flat gypsum substrate, the tilting of the layers due to the step modulates the microplatelets orientation in the horizontal plane. The varying in-plane microstructure can also be visualized macroscopically with the change in colors that depends on the microplatelets' orientation. Cutting the specimen as shown in Fig. 6 and looking at the cut cross-section indeed revealed alternating layers.

The variability among the specimens of the same step size could be due to some variation during the cutting and polishing of the samples. Nevertheless, this in-plane modulation is expected to impact the performance of the specimen, as the microplatelets may be able to deflect the cracks into more complex patterns. Interestingly, the samples resembled knots in wood which usually act as defects and decrease the modulus. Yet, the complex microstructure found in wood is thought to be responsible for the crack arrest at the edge of the knots. Bioinspired samples inspired from knots in woods have been produced to show crack arrest.[21] Therefore, the in-plane modulation of the microstructure could play a significant role in the crack propagation and the resilience of the composites.

Furthermore, to verify the microplatelet orientation in the constructs, the segments were fractured and observed under SEM (Fig. 7). The microstructural arrangement indeed reveals the curved layers and the 90° angle between the microplatelets in alternating layers. The cross-section of segment A obtained from gypsum with $h_{step} = 8$ mm was color coded using OrientationJ to show magnetic orientation in the different layers (Fig. 7). The layers with platelets which were aligned $\theta = 0°$, were uniformly colored gray. In this specimen, the layers should have microplatelets parallel to the horizontal substrate colored red; however, some tilted slightly and hence colored yellow. The yellow regions were in the areas closer to the gypsum substrate, probably due to the non-homogenous nature of the magnetic field produced by the rotating magnet (see Supplementary Fig. 2 for a schematic of the curved magnetic field lines). As the middle of the magnet was the only region producing perfectly horizontal magnetic field lines, the lower portion of the sample was subjected to a tilted magnetic field towards the edge of the magnet. The platelets were also tilted as a result.

Overall, alumina-PDMS composites with an unusually complex microstructure were produced. The microplatelet orientation of these samples was modulated not only along the vertical direction but also in-plane. To verify the hypothesis that
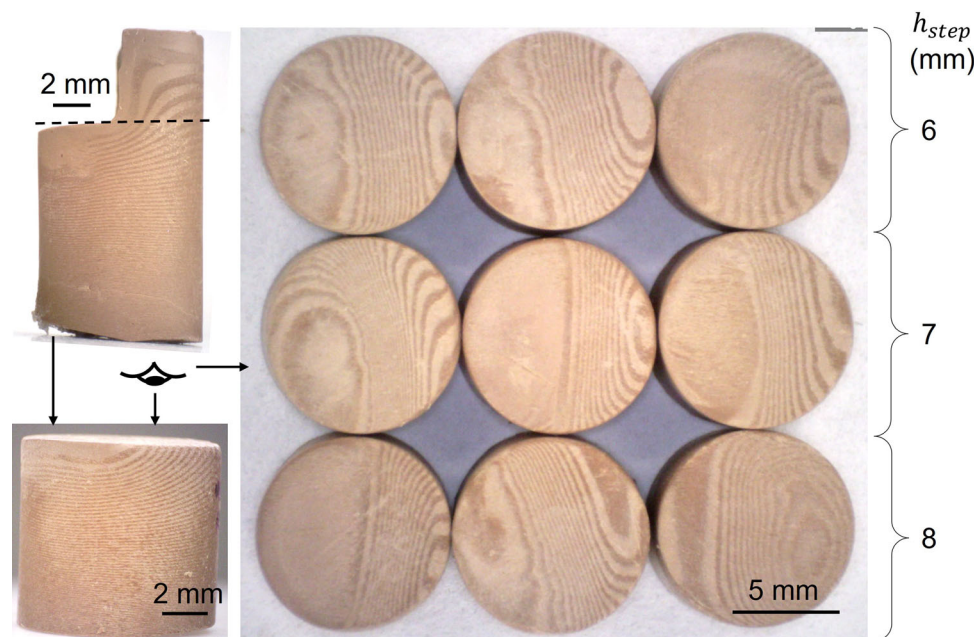
Fig. 6. Optical images of the layer patterns. The curved layers on the external surfaces were also visible in the cross-section after polishing.

increasing the microstructural complexity could improve the mechanical properties, the samples were tested under compression. Compression tests were selected because they could at the same time record the macroscopic mechanical behaviour and show insight into the cracking, as observed in other porous brittle materials like rock, gypsum, and concrete.[22–24]

Compression Properties

The porous multilayer microstructures obtained after MASC were infiltrated with PDMS as the polymer matrix. This polymer was chosen because of its weak properties as compared to the alumina, therefore enabling the study of the effect of the microstructure, mostly. Indeed, from our previous study on microstructured alumina-PDMS composites with planar multilayers, we could observe the samples cracking during compression, with almost no plasticity.[15] The samples obtained were first divided into segments B and A and tested under compression (Fig. 8). The semi-circular cross-section of segment A was taken into account in the measurement of the stress (Fig. 8A).

Since the microstructure of segment A did not vary with the step size, the tallest samples made using steps 6 to 8 mm were chosen for compression testing. The segment B samples made using a step height of 6, 7, and 8 mm were tested and compared with samples made with no step. Samples with these step heights were chosen as the samples with lower step heights had an insignificant amount of curvature in the layers. All the engineering stress–strain curves had generally similar profiles, with an elastic region followed by a short plastic region

before a peak and a drop in compressive stress that generally did not reach 0. The compressive behavior of these samples was also similar to the samples in the previous study, where the samples were cast on a flat surface. In the previous study, the samples made with alternating horizontal and vertical layers had a σ_{max} of about 3 MPa and failed at the strain of about 0.05.[15] In comparison to samples with no steps (Fig. 8B–F), segment A samples had a steeper slope in the elastic region of the stress–strain curves showing that the samples were stiffer. Also, the segment A samples exhibited stress–strain curves with a less sharp peak, suggesting a less abrupt fracture and increased apparent plasticity. However, there was no distinguishable difference between the segment B samples made with different step sizes 6 to 8 mm, which also looked similar to the samples made with no step. This is likely due to the layers being only slightly tilted whereas the curvature of the layers in segment A was pronounced.

Based on these results, we gathered the data into three groups: the samples with no step, the samples of segment B of varying step size, and the samples of segment A, and compared their stiffness, yield strength, deformation and energy dissipation (Fig. 9).

First, there were no significant differences between the elastic moduli of the multilayer samples with no step and the segment B samples (Fig. 9A). This is likely due to the similar layer height and orientation between these samples. However, there was a significant difference between the samples with no step and the segment B samples with the segment A samples ($p < 0.05$). The elastic modulus of segment A was
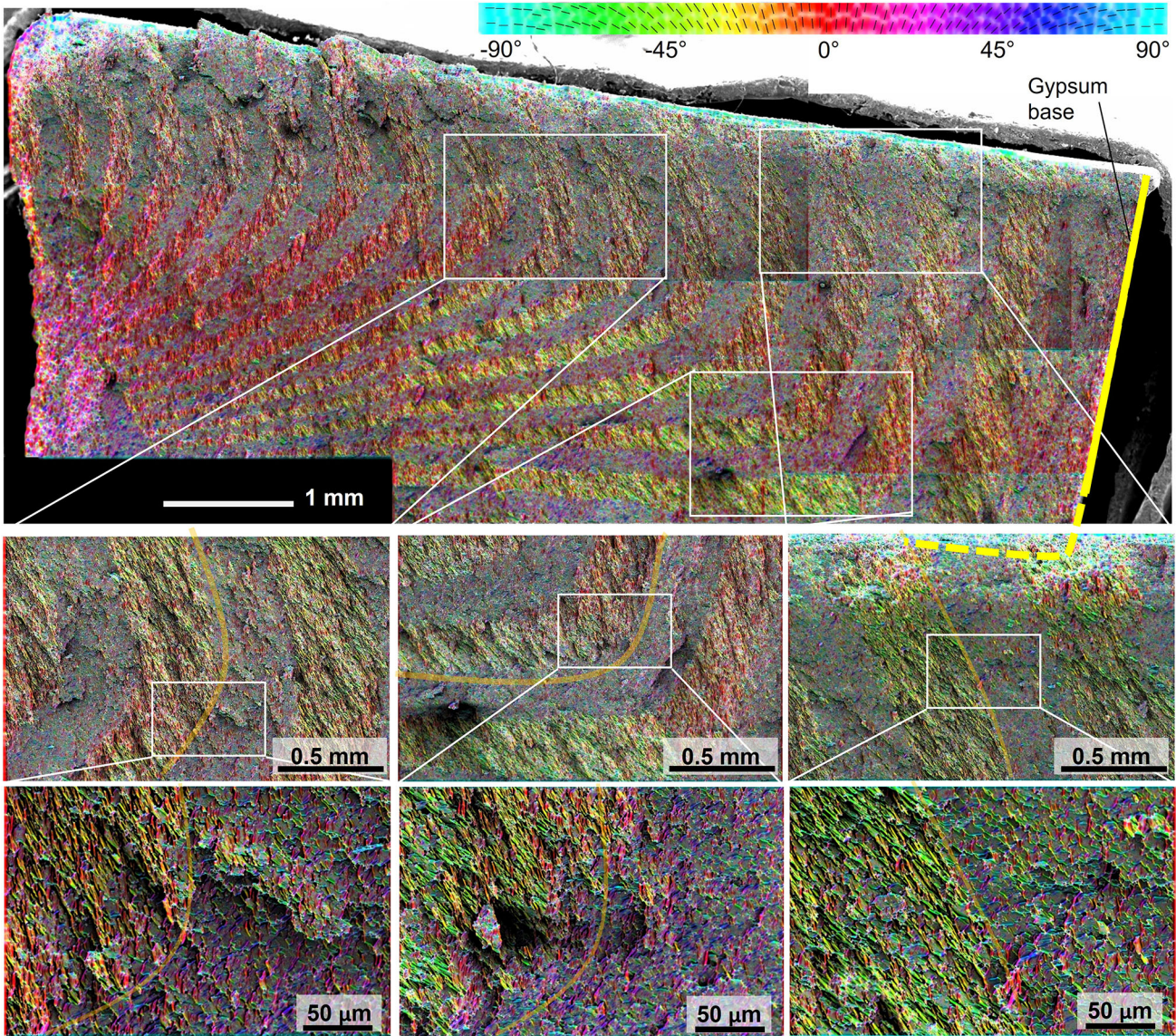
Fig. 7. Electron micrographs of the cross-section of a segment A sample, color coded using OrientationJ: lower magnifications showing the L-shaped layers following the contour of the gypsum base, and higher magnifications, showing the layer boundaries and alignment of the platelets in each layer. The alignment of the platelets is represented by the colors as shown in the color bar (Color figure online).

189.5 ± 3.3 MPa, significantly higher than that of segment B samples, of 85.4 ± 8.9 MPa and samples with no steps, of 93.2 ± 3.5 MPa. This shows that the segment A samples were about twice as stiff as the other samples. This increase in the stiffness is likely due to the microstructure in segment A where a number of layers exhibit vertically aligned microplatelets. Indeed, the modulus of samples of the same composition with purely vertically oriented microplatelets was reported to be about 280 MPa.[15] Therefore, it seems that the vertical layers in the segment A samples contributed mostly to the high stiffness. Since the samples A are made of both horizontal and vertical layers, and the other samples have only horizontal layers, the basic rule of mixture indeed confirms that samples A should be stiffer. To verify this, we also prepared samples with

pure vertical layers and tested them under compression (see Supplementary Fig. 3) and obtained a modulus of 312.7 ± 18.2 MPa. Assuming the samples A are 50% horizontal layers (93.2 ± 3.5 MPa) and 50% vertical layers (312.7 ± 18.2 MPa), the rule of mixture therefore predicts a modulus of about 200 MPa which is close to what was obtained experimentally.

This is interesting because, according to Fig. 7, the vertical layers were only occurring next to the gypsum step and spanned less than halfway across the cross-section.

Furthermore, for all the other compressive properties measured, the segment B samples exhibited the highest strength, strain and energy dissipated, but no statistical significance was found (Fig. 9B–D). σ_{yield} of all samples ranged from
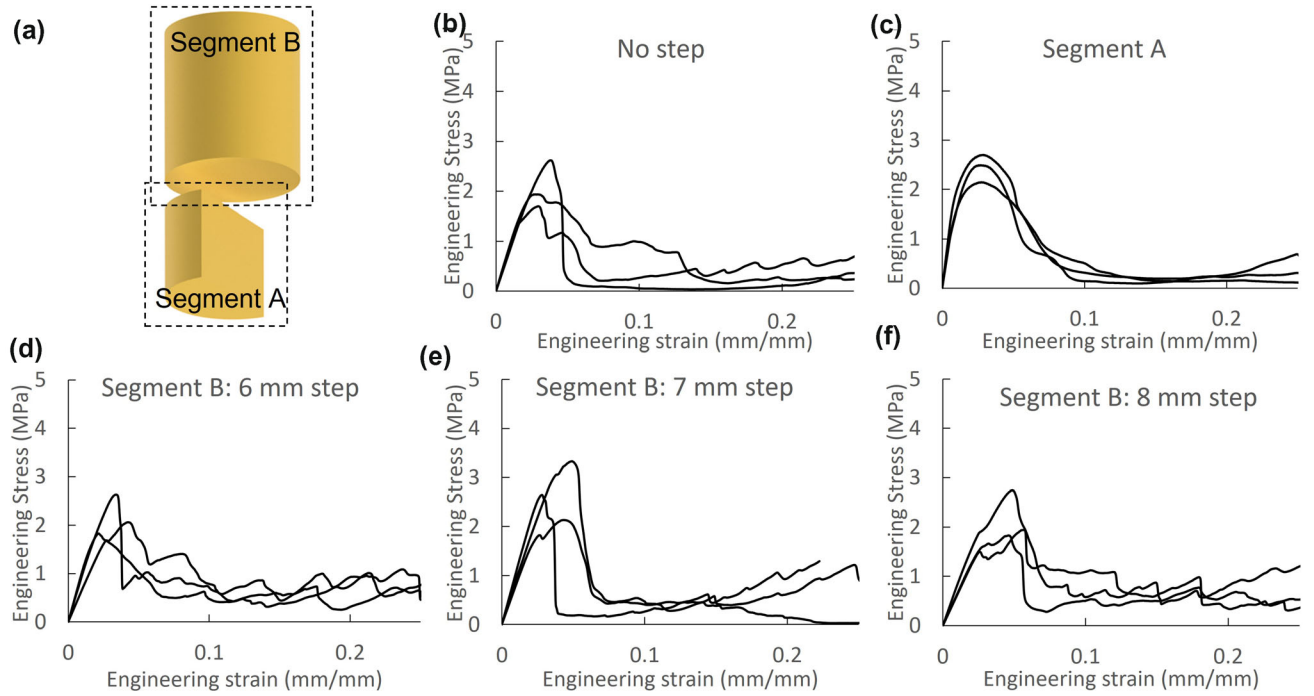
Fig. 8. (A) Schematic of a cast sample and the separation of segment A from segment B, where segment A's cross-sectional area is half of segment B's. Compression stress–strain curves of the microstructured samples with no steps (B), from segment A (C), and from segment B with 6-mm step size (D), segment B with 7-mm step size (E), and segment B with 8-mm step size (F).

1.85 ± 0.17 MPa to 1.61 ± 0.03 MPa, while ε_{yield} at ranged from 1.04 ± 0.29% to 2.40 ± 0.14%, showing minimal deformation in the elastic region. σ_{max} for samples with no steps, segment B, and segment A were 2.08 ± 0.24 MPa, 2.35 ± 0.26 MPa, and 2.26 ± 0.10 MPa, at the ε_{max} of 3.22 ± 0.25%, 4.13 ± 0. 56%, and 2.76 ± 0.02%. Respectively. σ_{yield}, ε_{yield}, σ_{max}, and ε_{max} all contribute to the work carried out on crack initiation, $E_{pre-crack}$, which was also very similar between the different groups, ranged from 42.2 ± 6.6 kJ/m^3 to 59.9 ± 11.0 kJ/m^3. This shows that the presence of the step feature did not prevent brittle behavior during the crack initiation region under compression. These values were, however, higher than for monoliths, with all platelets in the samples aligned vertically or at 45° to the horizontal, as reported previously to have $E_{pre-crack} < 30$ kJ/m^3.[15]

Finally, there was also little difference in the compressive properties of the samples with and without steps during crack propagation, ε_{fail}, at which a dramatic drop in the stress was recorded, were very close at 8.23 ± 2.3%, 9.73 ± 0.70%, and 12.66 ± 3.72% for samples with no steps, segment A, and segment B, respectively. E_{crack}, which is the energy dissipated during cracking, varied more between groups, with values of 57.8 ± 26.2 kJ/m^3, 87.7 ± 5.3 kJ/m^3, and 79.5 ± 30.1 kJ/m^3 for samples with no steps, segment A, and segment B, respectively. However, no statistical significance was found between these values. Therefore, the step in the gypsum substrate created curved features that did not significantly affect the overall toughness of the samples. This is actually surprising, as vertical orientations usually lead to lower toughness. From Fig. 10A, it can be seen that the σ_{max} and ε_{fail} of all the multilayered samples fall between that of the monolithic samples, showing that they simply possess a good combination of the strength and deformation of the monolithic samples with extreme properties. Considering the increase in stiffness in the segment A samples, however, shows that a prominent curvature in the multilayers increases the overall energy dissipated, given by the sum of $E_{pre-crack}$ and E_{crack} (Fig. 10B). Therefore, the curved structure in the layers observed in the segment A sample helped in combining high stiffness and high toughness within the same material, beyond that of multilayered samples without a prominent curvature in the layers.

To further study the influence of the microstructure on the resilience of the samples, we recorded the crack propagation during the compression tests and qualitatively discussed the failure of the samples (Fig. 11).

Similar crack patterns were observed in samples with no step and segment B (Fig. 11A, B). The images show a relatively smooth crack propagating diagonally across the sample. This further agrees with the compression test results and shows that not only were the mechanical properties of the samples similar but that the crack pattern was also similar. This similarity is likely due to the curvature of the layers created by the steps being not very
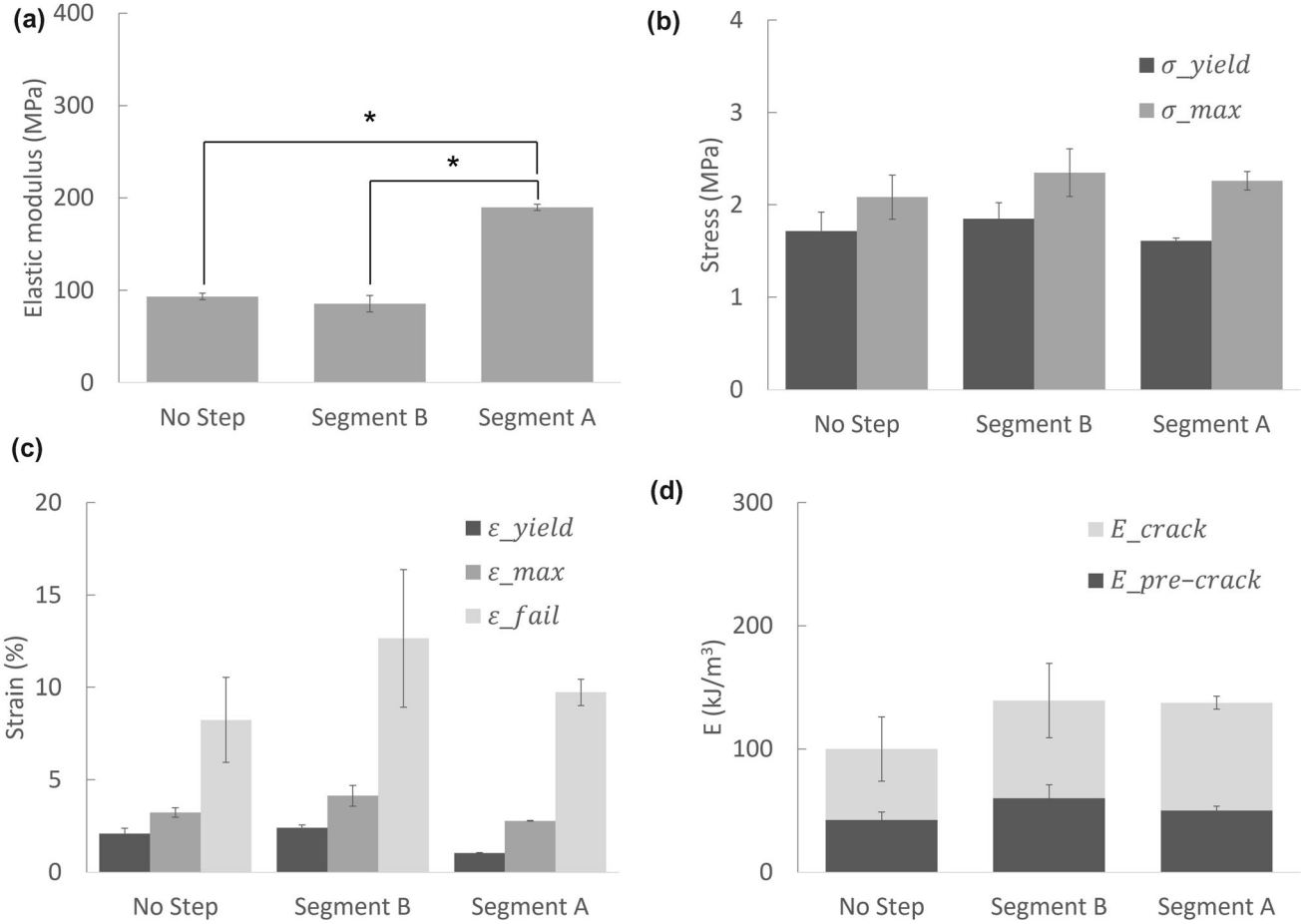
Fig. 9. Mechanical properties of the microstructured composites with curved layers: elastic modulus (A), yield σ_y and maximum stresses σ_{max} (B), strain at yield point ε_y, at the maximum stress ε_{max}, and at failure ε_{fail} (C), energy dissipated by cracking $E_{pre-crack}$ and during cracking E_{crack} (D).
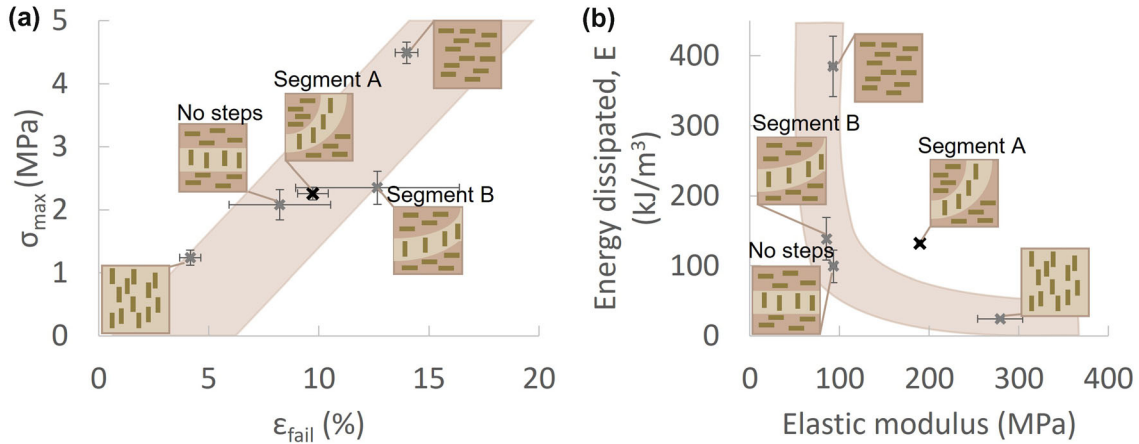

Fig. 10. Comparison of the mechanical properties between monolithic samples from previous work,[15] samples with no steps, segment A, and segment B samples. (A) The σ_{max} and ε_{fail} of all the multilayered samples generally fall between that of monolithic samples with vertical and horizontal alignments. (B) Segment A samples displayed a combination of toughness and stiffness which stood out compared to the other multilayered samples.

prominent. Hence, the segment B samples were structurally identical to the samples with no steps, and no difference could be found in the cracking behavior during compression. This result suggests that small misorientations in the sample have minimal effect.
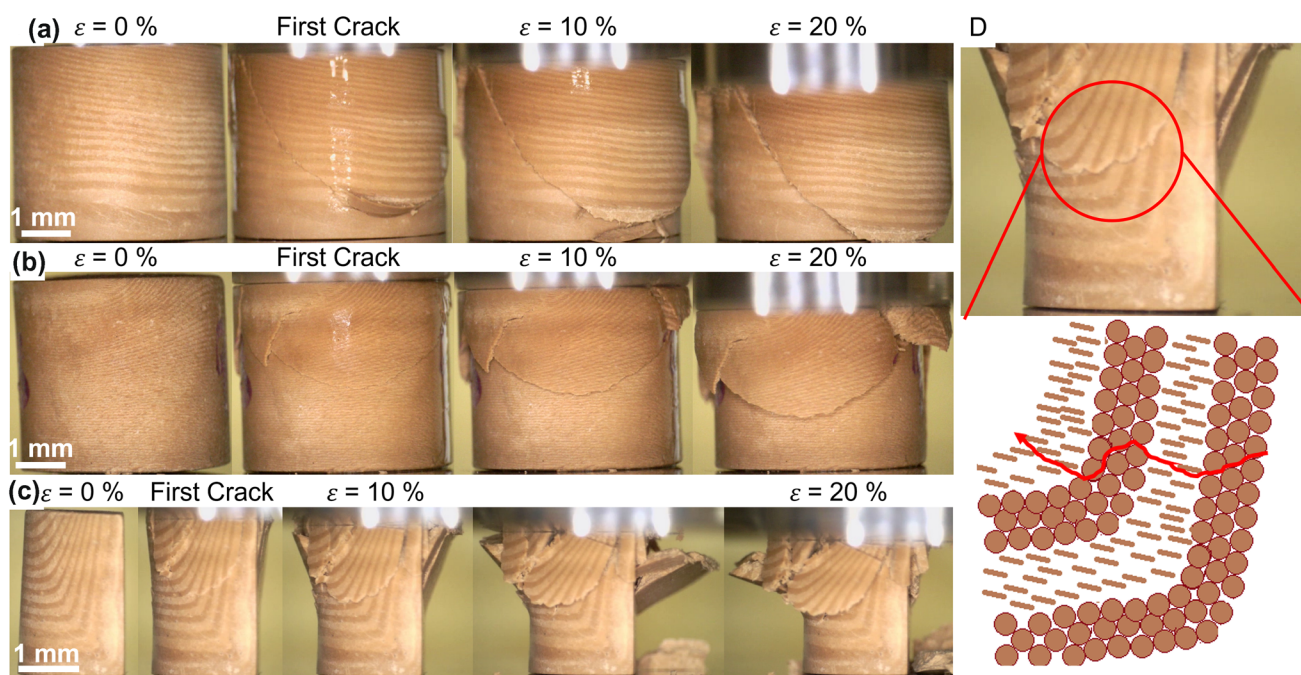
Fig. 11. Crack formation and propagation process in samples with no steps, a crack with a relatively smooth edge propagated diagonally through the sample (A), in segment B samples the crack was also relatively smooth diagonally across the sample (B), and in segment A sample the crack propagated with a ridged edge (C). (D) Deflected crack path in segment A sample and a schematic showing the crack propagating around the platelets.

However, samples from segment A displayed a different crack path (Fig. 11C). The samples showed straight vertical cracks in the region of the vertical layers, and tortuous ridged horizontal cracks in the region of the horizontal layers. This cracking pattern suggests that the vertical layers with λ close to 0° were fragile and did not deflect the cracks, where extensive crack deflection occurred in the curved regions and horizontal layers. These qualitative results, therefore, suggest that the horizontal layers contributed to the energy dissipation by effective deflection of cracks within its complicated microstructure.

From the compression tests and crack behavior, it can hence be concluded that prominent curves in the layers improved the stiffness of microstructured composites under compression. This could be a useful property in future developments of such composites, but there remain some limitations of this method, which will be discussed in the following section.

DISCUSSION

Curved Multilayers to Combine the Best Properties of Vertical and Horizontal Multilayers

Crack deflection is one of the toughening mechanisms in microstructured materials.[3] In composites with a soft matrix and hard filler, where a much higher amount of energy is required for the cracks to travel through the filler, the cracks are deflected

to travel in the matrix and interface between the two materials. A higher amount of energy is required for cracks to travel in the deflected path compared to the original path, and also the deflection increases the distance traveled by the crack, therefore increasing the work done in cracking, and leading to toughening. In this study, crack deflection caused by the microstructure of the sample was most pronounced in segment A, as evident in the formation of a ridged crack edge. Despite this, there was no significant difference in the toughness of segment A compared to segment B and samples with no steps. This was likely due to the compounded effects of stiffening and toughening due to the microstructure of the sample. Although there were variations in the measured mechanical properties, likely due to the polishing process during manufacturing, the results presented are representative and reproducible.

Multilayer samples with straight and vertical layers show delamination between the layers when compressed vertically, resulting in low toughness (see SI Supplementary Fig. 3 for images and compression stress–strain curves of those samples). This is because, during the unconfined compression test, the sample expands in directions perpendicular to the load, hence creating tensile forces leading to delamination. As a result of the curved layers, segment A samples have no straight vertical segments with in-plane modulation of vertical and horizontal layers. The region with vertical layers could have contributed to the increase in stiffness,

while the region with horizontal layers likely contributed to the toughness. As the crack traveled between regions of vertical and horizontal alignment, the crack direction changed, hence increasing the length of the crack path and leading to more toughening. Therefore, instead of having a rule of mixture between the mechanical properties of the horizontal and vertical multilayers, the composite with curved multilayers achieved the better properties of both, hence exhibiting both stiffness and toughness.

It is also interesting to note that the cracking of the segment A samples started from the periphery rather than the center although the transverse tensile stress resulting from compression is maximum at the center of the sample. In homogenous samples, the material is most likely to crack from the center, where local stresses are the highest. However, the samples in this study do not have a homogenous microstructure, and regions of weaknesses may be present in the peripheral layers due to the variation in the microstructure. Therefore, even with lower local stress levels, the cracking and delamination may occur first in these areas of weaknesses.

Although segment B also had curved layers, there was neither a difference in stiffness nor energy dissipated compared to samples without steps. This could be because the curvature was not prominent, resulting in a microstructure that was fundamentally identical to samples with no steps. The similarity between segment B and samples with no steps could also have been further increased by the small tilt angle, λ, due to the magnet's magnetic attraction during MASC. Therefore, the mechanical properties and crack patterns in segment B and samples with no steps were similar, suggesting that the curvature has to be more prominent than those in segment B to have stiffening effects, further confirming the above discussion.

Remaining Questions

There were some other factors not sufficiently explored in this study, which could have influenced the mechanical properties and crack patterns of the samples, such as the sample geometry and pitch. Although no significant differences were found between the samples without steps and samples in the previous study, the samples in this study had a larger diameter and a smaller pitch. These factors could have had an influence on the mechanical properties individually, but the effects could have been hidden as they were not tested. Studies on different materials have found that the cross-section geometry of samples does not affect the accuracy of compression tests.[25,26] However, the size has been known to have effects on the compression test results. Further tests will be required to isolate these variables and explore their individual effects on the mechanical properties of the samples.

The formation of the layers was highly dependent on the gypsum's water absorption rate. While it is known that gypsum absorbs water by capillary forces, the exact factors affecting the rate of water absorption, such as the volume of the gypsum, the porosity, and the ambient moisture level, and methods for controlling them, have not been well studied. Hence, while care has been taken to prepare every piece of gypsum with the same procedure, there may still be slight differences in the rate of water absorption of the gypsum, leading to a slightly different pitch across the samples. Hence, it may be useful to use other methods for the production of these samples, such that the formation of the layered structures is no longer dependent on gypsum, or to use other porous materials like polymeric molds.[27,28]

Due to the fragile nature of the samples, they were manually polished, and this inevitably resulted in some slight unevenness on the polished surfaces. Unfortunately, the in-plane distribution of the layers is very sensitive to the evenness of the polished cross-section, and slight unevenness can cause seemingly large variations in the layer pattern (Fig. 6). Nevertheless, from the mechanical test results, the variation between the samples is significantly less pronounced, and this shows that some surface unevenness may not affect the mechanical properties of the samples significantly. In future studies, a stronger polymeric phase could be added to strengthen the material, such that machine polishing can be used, allowing more accurate and precise levelling of the sample surfaces.

In addition, although it has been well established that crack deflection plays a part in improving the toughness of the material, the exact effects of how they propagate through the platelets with different alignments, and through the boundary of the layers with different alignments, have not been well studied. Under compression loading, mixed-mode fracture occurs within the sample, further complicating the actual crack propagation mechanisms.[29,30] Indeed, it is difficult to fully explain the crack energy dissipation phenomenon observed in such complex microstructures through simply studying the energy absorbed in different phases of cracking in the material. Mathematical modeling may help us to better understand the mechanism behind the cracking behavior observed. Alternative methods such as in situ X-ray tomography conducted during the compression testing may allow us to observe the cracking behavior of the samples with higher accuracy and with more detail.[31–33] This would help us to understand the fracture mechanisms of complex microstructured composites.

Towards the Production of Larger Specimens Through this Strategy

Production of complex structures using this method may be hindered by the size of the sample. In MASC, the gypsum's water removal rate drastically reduces as a function of the distance from the gypsum. When taller samples are made, much longer time is required, and, eventually, the production of larger samples will become prohibitively slow. The curvature of the layers in the samples also becomes less significant in layers further from the contoured gypsum base. Even if larger samples could be made, the curvature of the layers closer to the base cannot be replicated on the layers which are further away. Hence, the current production method is currently suitable only to produce thin samples. The complexity of the base gypsum contour is also limited by the need to de-mold the sample after slip casting. A complex base gypsum design may create delicate parts which break easily. This will cause the demolding process to become more difficult, and intricate designs may therefore not be achievable. Special design considerations will be needed to ensure the successful production of different geometries.

To overcome these limitations of MASC, it may be possible to create such complex microstructures using 3D printing augmented by magnetic orientation. Digital light processing has been used in conjunction with magnetic fields to produce microstructured composites with voxelated orientation control.[34] However, these use low concentrations of about 10–15 vol.% microplatelets, whereas our MASC samples had more than 35 vol.% platelets. Complex in-plane microparticle modulations with herringbone and mosaic alignment patterns could be realized, and notched samples were tested under tension to observe the crack path.[35] It was also found that highly complex microstructures lead to a large increase in fracture energy due to multiple deflection events. Another method to microstructure composites with high microplatelet content is magnetically assisted drop-on-demand 3D printing, where liquid droplets were concentrated using sedimentation, while the microplatelets were oriented with a low magnetic field.[36] Complex voxelated and highly reinforced composites produced by this method showed multiple crack deflections under compression tests. Other methods could also be explored to create locally varying microstructures, such as freeze-casting, acoustic fields, virtual magnetic molds, etc.[4] Finally, the mechanical properties measured here are very modest due to the nature of the weak matrix of PDMS. To achieve enhanced properties for structural applications, a stronger matrix than PDMS could also be used, such as tough epoxy, and computational methods could be used to optimize both composition and microstructure to achieve the best properties for a specific applications.[37]

CONCLUSION

By including the step feature in the gypsum mold during MASC, samples with curved layers could be created. The curved layers on the cast samples followed the contour of the gypsum mold. An increase in the height of the step feature increased the curvature in the cast sample, but, beyond a step height of 7 mm, no significant increase in the tilt angle, θ, was found. The curvature also became less prominent in regions further from the gypsum. Each cast sample consisted of segment B with slightly curved layers and segment A with a prominent curve in the layers. On the one hand, segment B was structurally similar to samples with no steps, and there was also no significant difference between the mechanical properties of segment B and samples made without a step. On the other hand, segment A was found to possess higher stiffness for the same toughness as segment B and samples with no step. This shows that complex microstructuring with curved multilayers and in-plane modulation was effective in augmenting the properties of the composites. In particular, the combination of vertical and horizontal layers and vertical and horizontal microplatelet alignments within these layers in the same composite leads to the combination of the high stiffness from the vertical microplatelet alignment in the vertical layers with the high toughness from the horizontal layers. This microstructural design could be applied to make bioinspired materials with superior stiffness and toughness.

AUTHOR CONTRIBUTIONS

XYC: Conceptualization, methodology, software, visualization, writing—review and editing. ZHN: Investigation, data curation, visualization, writing—original draft. LG: conceptualization, visualization, writing—review and editing. HH: Conceptualization, visualization, writing—review and editing. SS: Methodology, visualization, writing—review and editing. PD: Methodology, visual-

ization, writing—review and editing. HLF: Conceptualization, visualization, formal analysis, review and editing, supervision, funding acquisition.

CONFLICT OF INTEREST

REFERENCES

1. A. Ghazlan, T. Ngo, P. Tan, Y.M. Xie, P. Tran, and M. Donough, *Compos. Part B Eng.* 205, 108513 (2021).
2. S.E. Naleway, M.M. Porter, J. McKittrick, and M.A. Meyers, *Adv. Mater.* 27, 5455 (2015).
3. U.G.K. Wegst, H. Bai, E. Saiz, A.P. Tomsia, and R.O. Ritchie, *Nat. Mater.* 14, 23 (2015).
4. H. Le Ferrand, *J. Mater. Res.* 34, 169 (2019).
5. H. Zhao, Z. Yang, and L. Guo, *NPG Asia Mater.* 10, 1 (2018).
6. F. Bouville, *J. Mater. Res.* 8, 1 (2020).
7. P. Ramos-Silva, D. Wall-Palmer, F. Marlétaz, F. Marin, and K.T.C.A. Peijnenburg, *J. Struct. Biol.* 213, 107779 (2021).
8. S. Kamat, X. Su, R. Ballarini, and A.H. Heuer, *Nature* 405, 1036 (2000).
9. S. Amini, M. Tadayon, J.J. Loke, A. Kumar, D. Kanagavel, H. Le Ferrand, M. Duchamp, M. Raida, R.M. Sobota, L. Chen, S. Hoon, and A. Miserez, *Proc. Natl. Acad. Sci. U. S. A.* 116, 8685 (2019).
10. N. Suksangpanya, N.A. Yaraghi, R.B. Pipes, D. Kisailus, and P. Zavattieri, *Int. J. Solids Struct.* 150, 83 (2018).
11. K. Wu, Z. Song, S. Zhang, Y. Ni, S. Cai, X. Gong, L. He, and S.H. Yu, *Proc. Natl. Acad. Sci. U. S. A.* 117, 15465 (2020).
12. R.P. Behera and H. Le Ferrand, *Matter* 4, 2831 (2021).
13. H. Yazdani Sarvestani, D. Aranguren van Egmond, I. Esmail, M. Genest, C. Paquet, and B. Ashrafi, *Adv. Funct. Mater.* 32, 2108492 (2022).
14. G. Karambelas, S. Santhanam, and Z.N. Wing, *Ceram. Int.* 39, 1315 (2013).
15. X.Y. Chan, C. Chua, S. Tan, and H. Le Ferrand, *Compos. Part B Eng.* 232, 109608 (2022).
16. H. Le Ferrand, F. Bouville, T.P. Niebel, and A.R. Studart, *Nat. Mater.* 14, 1172 (2015).
17. H. Le Ferrand, *J. Eur. Ceram. Soc.* 41, 24 (2021).
18. H. Le Ferrand and F. Bouville, *J. Am. Ceram. Soc.* 102, 7253 (2019).
19. V.H.Y. Chou, W.C. Liu, M. Wittwer, H. Le Ferrand, and M. Seita, *Acta Mater.* 229, 117798 (2022).
20. R.P. Behera, S.B.S. Muhammad, M.H. Jiaxuan, and H. Le Ferrand, *J. Eur. Ceram. Soc.* 41, 617 (2021).
21. D. Kokkinis, F. Bouville, and A.R. Studart, *Adv. Mater.* 30, 1 (2018).
22. M.A. Tasdemir, A.K. Maji, and S.P. Shah, *J. Eng. Mech.* 116, 1058 (1990).
23. X. Xi, X. Wu, Q. Guo, and M. Cai, *IEEE Access* 8, 129636 (2020).
24. P. Cao, T. Liu, C. Pu, and H. Lin, *Eng. Geol.* 187, 113 (2015).
25. A. Talaat, A. Emad, A. Tarek, M. Masbouba, A. Essam, and M. Kohail, *Ain Shams Eng. J.* 12, 205 (2021).
26. C. Zhang, H. Lin, C. Qiu, T. Jiang, and J. Zhang, *Int. J. Damage Mech.* 29, 1076 (2020).
27. Y. Ergün, C. Dirier, and M. Tanoğlu, *Mater. Sci. Eng. A* 385, 279 (2004).
28. M. Yan, C. Zhou, X. Tian, G. Peng, Y. Cao, and D. Li, *Mater. Des.* 111, 198 (2016).
29. S. Suresh, C.F. Shih, A. Morrone, and N.P. O'Dowd, *J. Am. Ceram. Soc.* 73, 1257 (1990).
30. J. Tirosh and E. Catz, *Eng. Fract. Mech.* 14, 27 (1981).
31. G. Okuma, K. Maeda, S. Yoshida, A. Takeuchi, and F. Wakai, *Sci. Rep.* 12, 1 (2022).
32. Y. Wang, Y. Xiao, Z. Hou, C. Li, and X. Wei, *Arab. J. Geosci.* 13, 1018 (2020).
33. C. Löffl, H. Saage, and M. Göken, *Int. J. Fatigue* 124, 138 (2019).
34. J.J. Martin, B.E. Fiore, and R.M. Erb, *Nat. Commun.* 6, 1 (2015).
35. R.B. Zando, A. Mesgarnejad, C. Pan, S.J. Shefelbine, A. Karma, and R.M. Erb, *Compos. Sci. Technol.* 204, 108513 (2021).
36. W.C. Liu, V.H.Y. Chou, R.P. Behera, and H. Le Ferrand, *Nat. Commun.* 13, 5015 (2022).
37. J. Medinger, M. Nedyalkova, M. Furlan, T. Lüthi, J. Hofmann, A. Neels, and M. Lattuada, *ACS Appl. Mater. Interfaces* 13, 48040 (2021).